PROTEIN CONFORMATION FROM ELECTRON SPIN RELAXATION DATA

J. P. ALLEN, J. T. COLVIN, D. G. STINSON, C. P. FLYNN, AND H. J. STAPLETON
Department of Physics and Materials Research Lab, University of Illinois at Urbana-Champaign, Urbana, Illinois 61801

ABSTRACT Electron spin relaxation data from five ferric proteins are analyzed in terms of the fractal model of protein structures. Details of this model are presented. The results lead to a characterization of protein structures by a single parameter, the fractal dimension, d. This structural parameter is shown to determine the temperature dependence of the Raman electron spin relaxation rate, which varies as T^{3+2d}. Computations of d are made using x-ray data for 17 proteins. The results range from $d = 1.76$ for lysozyme to $d = 1.34$ for ferredoxin. These values are compared with values of d obtained from the present electron spin relaxation data on five ferric proteins. Typical results are $d = 1.34 \pm 0.06$ from relaxation data and 1.34 ± 0.05 from x-ray data for ferredoxin; $d = 1.67 \pm 0.03$ from relaxation data and 1.66 ± 0.05 from x-ray data for ferricytochrome c. The data thus support the theoretical model. Applications of this spin resonance technique to the study of changes in protein conformation are discussed.

I. INTRODUCTION

In this paper we present strong evidence that the fractal model of Stapleton et al. (1) provides an accurate description of Raman electron spin relaxation rates in ferric proteins. This model relates protein structure, as characterized by a fractal dimensionality d (2), and the density of vibrational states $\rho(\omega)$, which varies with frequency as ω^{d-1}, to the temperature dependence of the Raman relaxation process, which then varies as T^{3+2d}. Our model is generally applicable to systems of arbitrary fractal dimension d; it reduces to well-known results for structures such as paramagnetic salts, characterized by $d = 3$. Protein structures, however, are characterized by nonintegral values of d. The value of d can be calculated directly from x-ray structural data, or can be obtained alternately from the temperature dependence of the Raman relaxation rate, according to the theory discussed here. We have analyzed x-ray data for several proteins including ferricytochrome c with $d = 1.66 \pm 0.05$ and ferredoxin, with $d = 1.34 \pm 0.05$. Our model predicts that Raman relaxation rates in these proteins should vary as $T^{6.32 \pm 0.10}$ and $T^{5.68 \pm 0.10}$, respectively. Among the experimental data we present are results from three different research groups on ferricytochrome c and ferredoxin. The experimentally observed Raman relaxation rates in these two proteins vary as $T^{6.34 \pm 0.06}$ and $T^{5.67 \pm 0.11}$, in excellent agreement with our model.

Although the fractal dimensionality d is but a single parameter, it is nevertheless a useful indicator of protein conformation because it provides a quantitative measure of the degree to which a structure fills the space in which it resides. In this sense, it is, perhaps, less immediately accessible than other structural parameters, such as the radius of gyration, which can be measured optically. The polypeptide backbone of myoglobin meanders through space in such a way that its fractal dimensionality is 1.66 ± 0.04, according to x-ray data. This is very close to the theoretical value 5/3 associated with a self-avoiding random walk (SAW3) in three-dimensional Euclidean space (E3). A straight line backbone would have $d = 1$; if the backbone passed through every point of a lattice in E3, d would equal 3. This paper shows that the values of d can be measured by spin-lattice relaxation and x-rays to obtain identical results, and that changes in protein structure with solvent conditions can therefore conveniently be monitored by relaxation measurements.

In section II we review the early relaxation data on ferricytochrome c (cyt c) from horse heart (3) and cytochrome P-450 from *Pseudomonas putida* (P450) (4) which first indicated that electron spin-lattice relaxation rates of low-spin Fe^{3+} in proteins varied much more slowly with temperature than the expected T^9 power law. We also present new data for cyt c, lyophilized ferricytochrome c (cyt c-ly), low-spin myoglobin (Mb), myoglobin azide (MbN_3), and consider also the data of Gayda et al. (5) on ferredoxin. In section III we summarize the theory of Raman relaxation rates and extend it to include the vibrational spectrum of structures that have a nonintegral dimensionality. For structures of fractal dimension d, the resulting Raman relaxation rate of Kramer's ions (i.e., those with an odd number of unpaired spins) is found to vary with temperature as T^{3+2d}.

Fractal dimensions are discussed in more detail in section IV and a simple counting operation is described by which the dimension of a fractal structure can be determined. We then apply this technique to various proteins for

which x-ray structural data exist. In section V we use scaling arguments to prove that the vibrational density of states varies as ω^{d-1}. Section VI reviews some of the problems in the extraction of relaxation rates ($1/T_1$) from line width ($1/T_2$) data. Conclusions and acknowledgements appear in section VII.

II. RELAXATION DATA

General Results

As a result of experimental and theoretical research on electron spin-lattice relaxation over the past two decades, the various relaxation mechanisms and their characteristic temperature dependences are now rather well understood. Numerous review articles are available (6–9). It is of particular interest here that the Raman relaxation rates of all Kramer's doublets, such as low-spin Fe^{3+}, are known to vary with temperature T as T^9 at low temperatures. For covalently bound low-spin Fe^{3+} this has been confirmed using the diamagnetic crystalline host $K_3Co(CN)_6$ (10, 11). The first evidence that anomalies existed for Fe^{3+} spin relaxation in proteins appears to have been published in 1973 by Mailer and Taylor (3), who studied single crystals of ferricytochrome *c* at a microwave frequency of 24 GHz. Fig. 4 of reference 3 shows the data they used to obtain relaxation rates between 8 and 18 K. They used a novel technique that measured the phase lag of the resonance signal under conditions of adiabatic fast passage with high frequency magnetic field modulation. This phase lag manifests itself through a change in the output signal of a phase sensitive detector, larger than that expected for thermal spin populations. An unfortunate error occurred in the figure originally published, where the straight line drawn through the data was labeled as representing a T^7 power law. Only recently was it discovered instead that the line represents a $T^{6.0}$ variation with temperature. Nevertheless, neither T^7 nor T^6 behavior was anticipated by theory for this low-spin hemoprotein.

Additional evidence of unusual relaxation behavior in proteins, published in 1976 by Herrick and Stapleton (4), involved low-spin Fe^{3+} in frozen solutions of cytochrome *P*-450 from *P. putida*. These relaxation results, shown in Fig. 2 of reference 4, covered the temperature range from 1.75 to 13 K by means of a pulse-saturation/recovery technique. The low temperature Raman rate was again observed to vary with temperature much more slowly than the T^9 law. At that time, and based in part on the apparent fit of the Mailer and Taylor data in Fig. 1 to a T^7 law, the authors proposed a two-dimensional model to explain the results of spin-lattice relaxation data from hemoproteins. The rationale, which will be clarified by the theoretical development in section III, was that the T^7 variation could be associated with an effective phonon density of states that varies as the first power of frequency ω, rather than as ω^2. A linear dependence on frequency is characteristic of the state density in two-dimensional structures. Attention was drawn to a possible connection between this result and the planar structure of the heme group with which the iron is associated. Because the data for *P*450 fell below a strict T^7 dependence, it was necessary to include the appropriate transport integral (see section III) with a rather low Debye temperature of 75 K.

Recent data on additional systems established that a simple power law, of the form T^n, fits all these Raman relaxation data and that n is close to 6.3 for hemoproteins. Fig. 1 shows how well T^n fits the data for four low-spin ferric systems: *P*450 ($n = 6.27 \pm 0.06$), MbN_3 ($n = 6.29 \pm 0.08$), Mb (low-spin, liquid state pH = 11.7, $n = 6.22 \pm 0.09$), and cyt *c* ($n = 6.34 \pm 0.06$). Also shown in Fig. 1 is a straight line corresponding to a T^9 power law. It should be noted that the cyt *c* data in this figure combine our pulse-saturation/recovery data (limited to rates under $10^4\ s^{-1}$), taken on a frozen solution (liquid state pH = 6.8) up to a temperature of 8.5 K, with the Mailer and Taylor data from single crystals of cyt *c* between 11 and 18 K. This determines n more accurately. It proved necessary to reduce the phase-lag rates by a factor of 0.106 to bring the two sets of data into agreement.

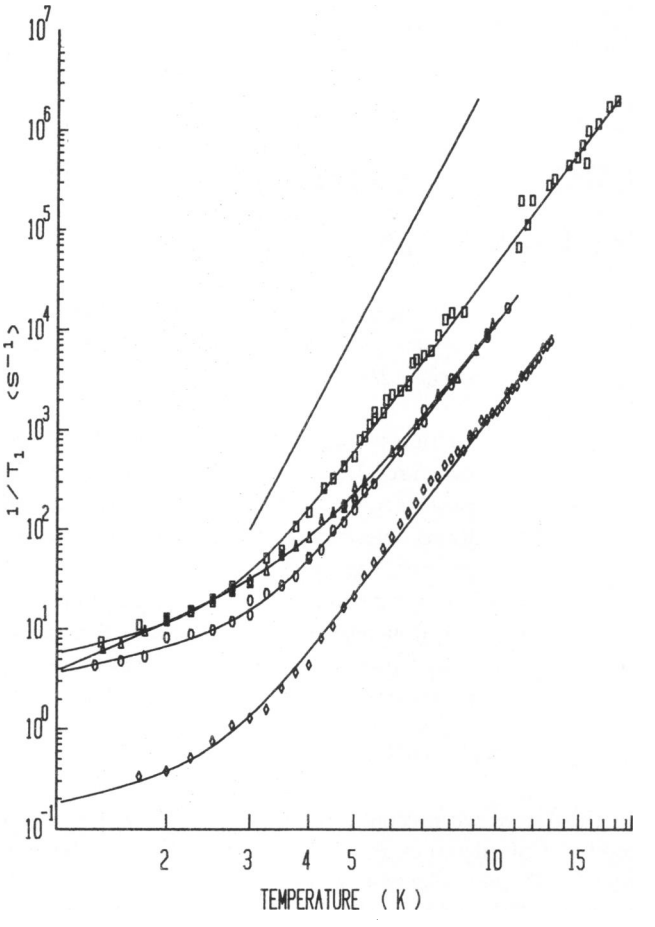

FIGURE 1 Relaxation rates for four low spin hemoproteins from this work and references 3 and 4. The data from cyt c (□, $1/T_1 = 4.85T + 0.0221T^{6.34}$), Mb (Δ, $1/T_1 = 2.79T^2 + 0.007267T^{6.22}$), MbN_3 (○, $1/T_1 = 3.11T + 0.00617T^{6.29}$), and P450 (◇, $1/T_1 = 0.152T + 0.000910T^{6.27}$) are separately fit to the sum of a direct process, varying with temperature as T or T^2, and a simple T^n power law. The best fitting values of n are indicated. Standard errors in n are typically 1%. The straight line represents a T^9 power law. For Mb and MbN_3, 2/3 of the data between 5 and 11 K are not displayed in order to improve visual clarity in the region of overlap. Every third point, determined sequentially by temperature, is shown. The straight line represents a T^9 power law.

It seems possible that the Mb result, $n = 6.22 \pm 0.09$, may represent a real change of protein conformation in the low-spin state in a highly basic solution. The remaining three systems yield an average value of $n = 6.30 \pm 0.07$. It will be shown below, on the basis of a fractal model of relaxation and of x-ray structural data from cyt *c* and high spin Mb, that a value of $n = 6.32 \pm 0.10$ is expected for these hemoproteins. We also present, in Fig. 2, the relaxation data of Gayda and co-workers (5) on a 2-iron-2-sulfur ferredoxin from the blue-green algae *Spirulina maxima*. This plot includes data obtained by pulse-saturation/recovery and continuous wave (cw) saturation only up to a temperature of 20 K, which eliminates the two highest cw relaxation rates from their original plot (one was only an estimated value). In contrast to the hemoproteins, the fit of a T^n power law to these Raman data now yields $n = 5.67 \pm 0.11$. We show below, using x-ray structural data on 8-iron-8-sulfur ferredoxin from *Peptococcus aerogenes*, that the fractal model proposed here predicts $n = 5.68 \pm 0.10$ for this iron-containing, nonheme protein.

Fig. 3 shows that the protein environment, as distinct from its structure, has no effect on the Raman relaxation rate. It does, however, influence the temperature dependence of the direct relaxation rate that

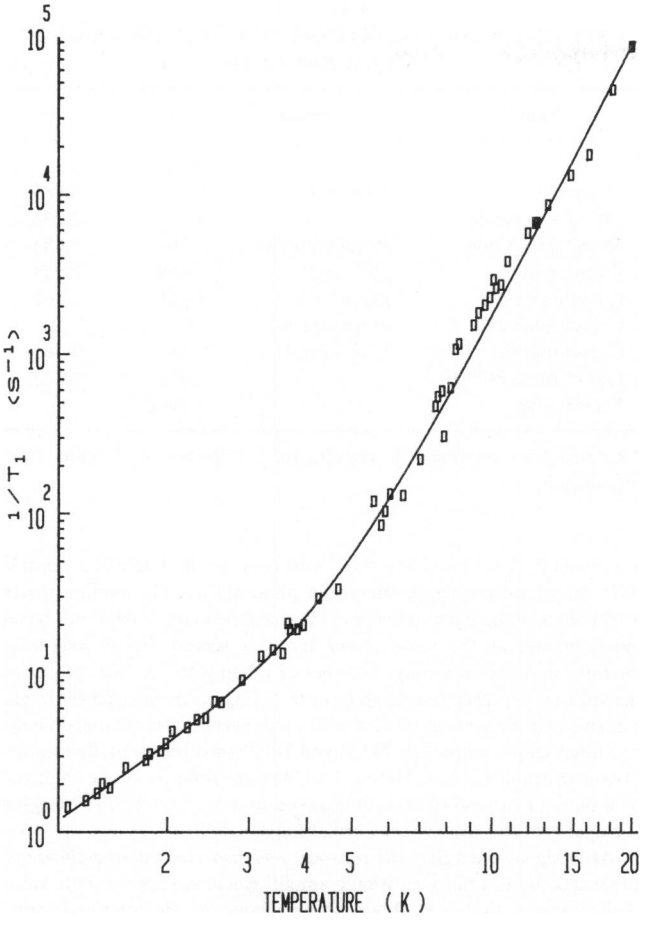

FIGURE 2 X-band relaxation data from reference 5 on a reduced 2-iron-2-sulfur ferredoxin from the blue-green algae *S. maxima*. Included are pulse-saturation/recovery data and overlapping cw saturation data. Our best fit of these data to the sum of T^2 and T^n power laws results in $n = 5.67 \pm 0.11$. This agrees closely with the fractal model that predicts $n = 5.68 \pm 0.10$ on the basis of x-ray structural data. Here, $1/T_1 = 0.861T^2 + 0.00359\ T^{5.67}$.

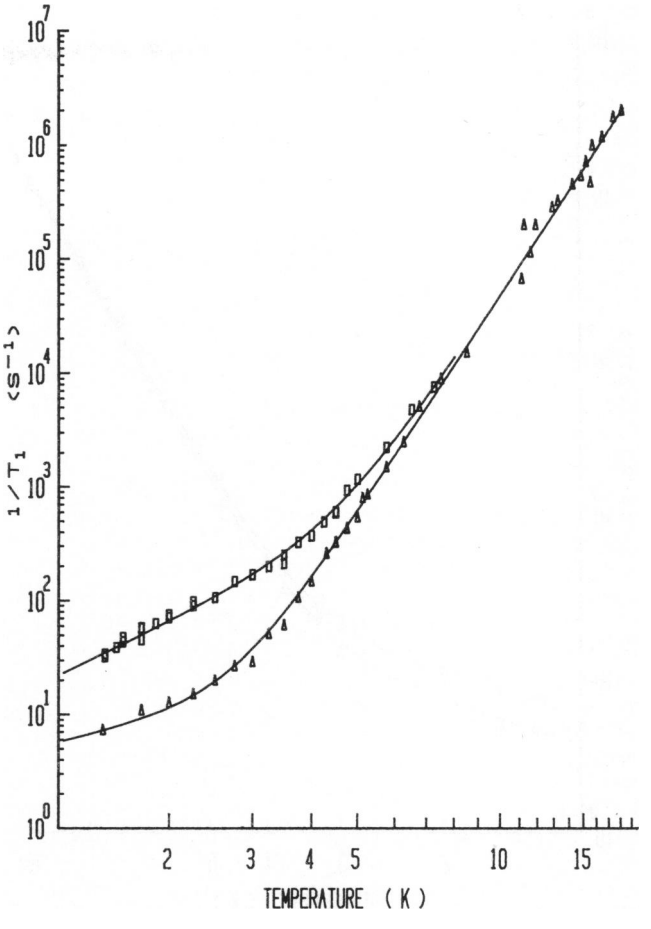

FIGURE 3 Data showing the effect of lyophilization on the relaxation rate of ferricytochrome *c*. Our data, corresponding to rates under $10^4\ s^{-1}$, correspond to a frozen solution of cyt c (Δ, $1/T_1 = 4.85T + 0.0221T^{6.34}$), and a lyophilized sample, cyt *c*-ly ($\square$, $1/T_1 = 16.1T^2 + 0.0241T^{6.333}$). The net Raman rates are within 7% of each other at $T = 8$ K. The effect of lyophilization is to change the direct relaxation rate from T to T^2 and to increase it by 664% at $T = 2$ K. For this figure, 2/3 of the data between 5 and 11 K are not displayed in order to improve visual clarity in the region of overlap. Every third point, determined sequentially by temperature, is shown.

dominates at the very lowest temperatures near 1 K. The lower curve of Fig. 3 is taken directly from the cyt *c* data in Fig.1 and therefore involves data from both a single crystal and the frozen solution. The upper curve of Fig. 3 shows our data for a freeze-dried sample of cyt *c*. In the fitting of relaxation data from this lyophilized sample, the Raman rate exponent was fixed at $n = 6.333$, which corresponds to a fractal dimension of 5/3. This was necessary because these data occupy only a limited temperature range. It is therefore apparent from the figure that the protein environment does not influence the Raman relaxation rate. At low temperatures, however, the relaxation rate of the freeze-dried sample exhibits a T^2, rather than T, temperature dependence. An identical temperature dependence occurs (Fig. 1) in the direct relaxation process for Mb in a highly basic, low-spin state and (in Fig. 2) for ferredoxin. The evidence therefore appears to establish that the protein environment affects the temperature dependence of the direct relaxation rate alone and does not influence the Raman process. If AT and DT^2 represent the unbottlenecked and the bottlenecked direct relaxation rate of a spin system, then the condition for a bottleneck is $DT^2 << AT$ (12, 13). Unless lyophilization drastically increases the spin-phonon coupling at the microwave frequency, the necessary inequality is not satisfied for cyt *c*. We are led to speculate that the relaxation may, instead, be due to the presence of localized tunneling states (14) created by the removal of water. It is known from microwave frequency dielectric absorption data on metmyoglobin crystals (15) that virtually all the water is adsorbed on the protein.

Further evidence that indicates that the Raman rate in these proteins is little affected by sample history is furnished by relaxation data from a reconstituted frozen solution of myoglobin azide (labeled MbN_3-R). These data are compared with our earlier results for MbN_3 in Fig. 4. The reconstituted sample was prepared by freeze-drying a frozen solution and then redissolving it. The two sets of relaxation data were taken by different researchers. Furthermore, the *g*-values and microwave frequencies given in Table I indicate that the two measurements were performed on slightly different portions of the frozen solution spectrum. Nevertheless, the temperature dependence of the Raman rates is unchanged within the experimental uncertainty because the two cases lead respectively to $n = 6.28 \pm 0.06$ and $n = 6.29 \pm 0.08$. Also, the magnitudes of the Raman relaxation rates agree to within 10%, and even this difference is probably associated with slight anisotropies in the Raman rate. For example, the measured Raman rates for MbN_3 at $g_{eff} = 2.21$ and 1.71 were respectively 1.5 and 2.5 times larger than at $g_{eff} = 2.75$. Attempts to measure relaxation rates on freeze-dried MbN_3 were unsuccessful because of the

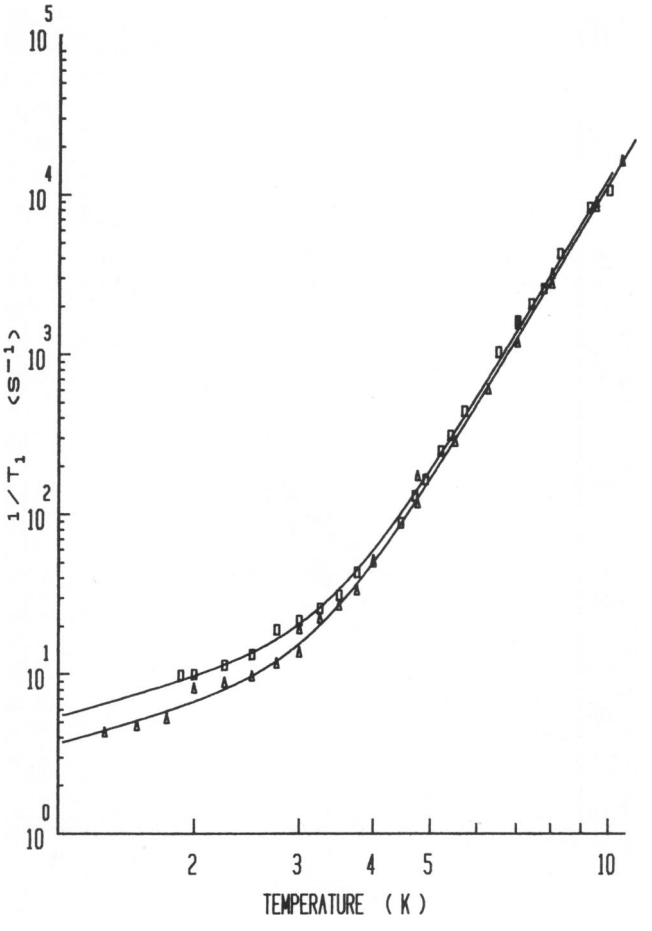

FIGURE 4 Data indicating the degree to which our relaxation measurements on frozen solutions of proteins are independent of sample history. Data shown along the upper curve involved a reconstituted frozen solution of myoglobin azide (MbN_3-R), which had had an additional stage of freeze-drying before use in the spectrometer (□). The standard errors in T^n Raman fits were 0.06 and 0.08 for the upper and lower curves, respectively. For this figure, 2/3 of the data between 4 and 11 K are not displayed in order to improve visual clarity in the region of overlap. Every third point, determined sequentially by temperature, is shown. □, MbN_3-R, $1/T_1 = 4.60T + 0.00688T^{6.28}$; △, MbN_3, $1/T_1 = 3.11T + 0.00617T^{6.29}$.

appearance of a substantial high-spin component in the EPR spectrum, and the fact that the overlap of low- and high-spin spectra leads to spin-spin relaxation through the Orbach process of the high-spin species.

An interesting result was also obtained from our relaxation measurements on cyt *c* in a frozen solution that had a pH of 13.2 prior to freezing. This corresponds to type V cyt *c* (16, 17), an unfolded, low-spin system, that is thought to have OH^- as the sixth iron ligand. Our relaxation data showed no evidence of a detectable Raman relaxation mechanism up to a temperature of 22.6 K where our measurements stopped. The relaxation rate varied no faster than T^2 over the entire range of our measurements.

Experimental Details

All of our relaxation measurements were made using the pulse-saturation/recovery technique. The spectrometer used broad-band (dc – 10 MHz) superheterodyne detection and signal averaging. Saturating pulses were generated by passing microwaves through a variable attenuator in series with a 50 dB solid-state microwave switch, shunted by a wave-guide arm containing two 15-dB cross-guide couplers, a variable 0–75-dB attenuator, and a microwave phase shifter. The monitor power level used to observe the recovery of the resonance signal could thus be set independently of the pulse power level. A second 50-dB solid-state microwave switch, operating 180° out of phase with the first, protected the sensitive superheterodyne receiver from high microwave power levels. The two switches were controlled with a pulse generator containing model 555 timer chips and models 74123 and 74121 monostable multivibrators (Texas Instruments, Inc., Dallas, TX). The generator could be triggered by a pulse at the end of each time sweep from a Fabri-Tek 1070 signal averager (Nicolet Instrument Corp., Madison, WI).

TABLE I
EXPERIMENTAL CONDITIONS FOR THE RELAXATION MEASUREMENTS

Sample	Comment	ν	g
		GHz	
Myoglobin	Low spin	9.374	1.865
Myoglobin Azide		9.251	2.754
Myoglobin Azide	Reconstituted	9.306	2.683
Cytochrome c	pH = 6.8	9.459	2.938
Cytochrome c	pH = 13.2	9.421	2.362
Cytochrome c*	Single crystal	24	–
Cytochrome c	Lyophilized	9.487	2.465
Cytochrome P-450‡		9.496	2.423
Ferredoxin§		x-band	–

*Results from reference 3; ‡results from reference 4, §results from reference 5.

After signal averaging, the recovery was displayed on an oscilloscope either directly or after logarithmic amplification. An approximate value of the relaxation rate was obtained immediately by the latter procedure. The contents of the Fabri-Tek memory were then transferred to paper tape or a magnetic floppy disk for subsequent analysis on a DEC-20/60 (Digital Equipment Corp., Maynard, MA) computer. The signal recoveries were truly exponential over the full recovery period only for the MBN_3 samples. The relaxation rates we report for other samples are representative of the recovery rates when the signal had returned to a value between 40 and 90% of its thermal equilibrium value. Care was taken to insure that the rates were independent of both the duration and the intensity of the saturating pulses.

The frozen protein solutions were in direct thermal contact with a cylindrical TE_{111} mode microwave cavity made from copper. Teflon baffles held the samples in regions of large H_1^2. The cavity was thermally insulated from a liquid helium bath by a thin-wall stainless-steel wave guide and by a surrounding vacuum-tight isolation can, made of brass, into which helium exchange gas could be introduced. The cavity temperature was measured with a calibrated germanium or carbon-glass resistance thermometer that was part of an ac bridge circuit. Error signals from the bridge circuit controlled the direct current (0–65 mA) in a 500-Ω heater coil wound around the cavity. Microwave coupling to the cavity was varied with a Gordon coupler (18).

Protein Preparation

Horse heart cyt *c* (type VI) and sperm whale Mb (type II) were purchased from Sigma Chemical Co., St. Louis, MO, and used without further chemical purification. MbN_3 was prepared by dissolving Mb in a pH = 7.0 phosphate buffer solution containing 0.5 M NaN_3 until a 10-mM concentration of Mb was reached. A 10-mM low-spin myoglobin solution was prepared by first dissolving it in a phosphate buffer of pH 6.8. The pH was then adjusted to 11.7 by slowly adding 1 M NaOH. A 10-mM solution of low-spin, folded cyt *c* was prepared by dissolving it in a

phosphate buffer of pH = 6.8. A 3-mM solution of low-spin, unfolded cyt *c* was prepared by dissolving it in hydrochloric acid and then changing the pH from 1 to 13.2 by the slow addition of a 1 M NaOH solution. All solutions were centrifuged to remove undissolved material.

To prepare a lyophilized sample of MbN_3, a frozen solution of it was held in vacuum for 36 h at a temperature of $-10°C$. The 10-mM solution of reconstituted MbN_3 was prepared by dissolving the lyophilized sample in a phosphate buffer of pH 7.1. A lyophilized sample of cyt *c* was prepared in a similar manner from a frozen solution, although the temperature, in this case, may have briefly reached room temperature. The EPR spectra of these samples were found to agree with published results (19–22).

III. RAMAN RELAXATION PROCESS

In the Raman relaxation mechanism, a high-energy phonon scatters inelastically off a paramagnetic spin and causes a spin flip and a corresponding change in the energy of the scattered phonon. This process is faster than the direct (one phonon) process when the temperature is high enough to populate the higher energy phonon states ($\hbar\omega >> g\mu_B H$). The two phonon process is dominant because all high energy phonons can take part while only those with energy $g\mu_B H$ are available for the direct process. Physically, the relaxation process involves a modulation of the ligand electrostatic field by structural vibrations. This perturbs orbital electronic states that are coupled to the spin via the spin-orbit interaction. In general there are two contributions to a two-phonon relaxation rate. One comes from the use of first-order time-dependent perturbation theory and an orbit-lattice Hamiltonian, $\mathcal{H}_{OL}$, which is second order in strain (i.e., second order in phonon creation and destruction operators). The other arises from the use of second-order time-dependent perturbation theory with an orbit-lattice Hamiltonian, which is first-order in strain. Only the second approach yields a nonzero result for a Kramer's ion, because the $\mathcal{H}_{OL}$ operator is time even and therefore cannot connect the two states of a Kramer's doublet. A weak H^2T^7 Raman rate is predicted for a Kramer's ion, but little confirming evidence has been reported (23, 24).

The critical factors in a computation of the Raman relaxation rate can be reproduced by adopting the following simplified, phenomenological orbit-lattice Hamiltonian:

$$\mathcal{H}_{OL} = \sum_{\ell} \vec{\vec{\epsilon}} : \vec{\vec{V}}_{\ell} = \sum_{\ell\sigma} \left(\frac{\hbar\omega_\sigma}{2Mv^2} \right)^{1/2} (b_\sigma - b_\sigma^\dagger) R_{\ell\sigma} V_\ell, \quad (1)$$

which, in the long wavelength limit, is closely related to that used by Orbach and Tachiki (25). In Eq. 2 $\vec{\vec{\epsilon}}$ is a strain operator and $\vec{\vec{V}}_\ell$ is a time-even tensor operator that acts upon electronic wave functions and has, for notational simplicity, a single index ℓ. Various phonon indices including polarization are included by a single greek index. $b_\sigma^\dagger$ and b_σ are creation and destruction operators for phonons of index σ. $R_{\ell\sigma}$ is a dimensionless, geometrical coupling factor between a phonon of index σ and the tensor component V_ℓ, but is independent of the phonon frequency ω_σ. M is the total mass and v is the velocity at which vibrations propagate in the protein.

The expression for the relaxation rate is

$$1/T_1 = W(1 \rightarrow \bar{1}) + W(\bar{1} \rightarrow 1), \quad (2)$$

where $W(n \rightarrow m)$ is the transition rate from $|n>$ to $|m>$ and $|1>$ and $|\bar{1}>$ are, in this case, the Kramer's conjugate states of the ground doublet. Because $W(1 \rightarrow \bar{1}) = W(\bar{1} \rightarrow 1)$ for a Raman process, the relaxation rate becomes

$$\frac{1}{T_1} = \frac{4\pi}{\hbar} \sum_f \left| \sum_m \frac{\langle f | \mathcal{H}_{OL} | m \rangle \langle m | \mathcal{H}_{OL} | i \rangle}{E_i - E_m} \right|^2 \delta(E_i - E_f), \quad (3)$$

where E_k is the energy of state k and $\delta(x)$ is the Dirac delta function.

The initial, intermediate, and final states $|i>$, $|m>$, and $|f>$ are each a product of electronic and phonon states. Because the intermediate phonon states can be created or destroyed in either order, there are four intermediate states to be included in the summation over m in Eq. 3 for each excited doublet $|j>$ and $|\bar{j}>$ of the Fe^{3+} ion. The pertinent states are

$$\begin{aligned} |i> &= |1>|....n_\mu \quad ....n_\lambda \quad ....> \\ |f> &= |\bar{1}>|....n_\mu - 1....n_\lambda + 1....> \\ |m\,1> &= |j>|....n_\mu - 1....n_\lambda \quad ....> \\ |m\,2> &= |\bar{j}>|....n_\mu - 1....n_\lambda \quad ....> \\ |m\,3> &= |j>|....n_\mu \quad ....n_\lambda + 1....> \\ |m\,4> &= |\bar{j}>|....n_\mu \quad ....n_\lambda + 1....> \end{aligned}, \quad (4)$$

where n_μ is the thermal phonon occupation number, $(e^{\hbar\omega_\mu/k_B T} - 1)^{-1}$.

If j and $\bar{j}$ are a pair of Kramer's conjugate states, Q is the time-reversal operator, and V_ℓ is a time-even operator (26), then

$$\begin{aligned} &QV_\ell Q^{-1} = V_\ell^\dagger, \quad Qj = \bar{j}, \quad Q\bar{j} = -j \\ &(\bar{1}, V_\ell \bar{j})(\bar{j}, V_{\ell'} 1) = (QV_\ell Q^{-1} Q\bar{j}, Q\bar{1})(QV_{\ell'} Q^{-1} Q\bar{1}, Q\bar{j}) \\ &\qquad = -(\bar{1}, V_{\ell'} j)(j, V_\ell 1). \end{aligned} \quad (5)$$

It is then easily shown that Eq. 3 becomes

$$\begin{aligned} \frac{1}{T_1} = \frac{\pi\hbar}{M^2 v^4} &\sum_{\mu\lambda} \omega_\lambda \omega_\mu n_\mu (n_\lambda + 1) \\ &\left| \sum_{j,\ell,\ell'} (R_{\ell\lambda} R_{\ell'\mu} - R_{\ell\mu} R_{\ell'\lambda}) \left(\frac{1}{\Delta_j - \hbar\omega_\mu} - \frac{1}{\Delta_j + \hbar\omega_\lambda} \right) \right. \\ &\left. \langle \bar{1} | V_\ell | j \rangle \langle j | V_{\ell'} | 1 \rangle \right|^2 \times \delta(\hbar\omega_\lambda - \hbar\omega_\mu - g\mu_B H), \end{aligned} \quad (6)$$

where Δ_j is the energy of the jth excited doublet. In the static limit, with ω_μ and ω_λ both zero, $1/T_1$ vanishes for

Kramer's ions. Because the pertinent phonon energies are nonzero, but are nevertheless much smaller than Δ_j, the energy denominators combine to yield $\hbar(\omega_\mu+\omega_\lambda)/\Delta_j^2$. The ω-independent coupling factor term, $|R_{\ell\lambda}R_{\ell'\mu} - R_{\ell\mu}R_{\ell'\lambda}|^2$ can now be averaged incoherently over polarization and spatial index (6) and removed from the summation (integration) over phonon modes. In addition the small frequency difference $\omega_\lambda - \omega_\mu = g\mu_B H/\hbar$ between the pertinent phonons can be ignored, so that our expression becomes

$$\frac{1}{T_1} = \frac{4\pi\hbar^2}{M^2 v^4} \sum_{\ell,\ell',j} \overline{(R_{\ell\lambda}^2 R_{\ell'\mu}^2 + R_{\ell\mu}^2 R_{\ell'\lambda}^2)_{\lambda\mu}} \; (|\langle \bar{1}|V_\ell|j\rangle\langle j|V_{\ell'}|1\rangle|^2)/(\Delta_j^4) \times \int_0^{\omega_{max}} \frac{\omega^4 \rho^2(\omega) e^{\hbar\omega/k_B T}}{(e^{\hbar\omega/k_B T}-1)^2}\, d\omega. \quad (7)$$

As we shall later prove, the density of vibrational states, $\rho(\omega)$, varies with frequency as ω^{d-1} where d is the fractal dimension. An evaluation of the integral in Eq. 7 then leads to the temperature dependence

$$\frac{1}{T_1} = T^{3+2d} J_{2+2d}(\Theta/T), \quad (8)$$

where $\Theta = \hbar\omega_{max}/k_B$ and $J_n(x)$ is a transport integral (27) defined as

$$J_n(x) \equiv \int_0^x \frac{z^n e^z}{(e^z-1)^2}\, dz. \quad (9a)$$

It has the limiting values

$$\lim J_n(\Theta/T) = n\Gamma(n)\zeta(n), \quad T << \Theta, \quad (9b)$$

and

$$\lim J_n(\Theta/T) \propto (\Theta/T)^{n-1}, \; T >> \Theta, \quad (9c)$$

where $\Gamma(n)$ is the Gamma function and $\zeta(n)$ is the Riemann zeta function.

These results reproduce the well-known dependence of Raman relaxation rates on temperature as observed in ordinary solids, i.e., $d = 3$, $T_1^{-1} \propto T^9$ at low temperatures, $T_1^{-1} \propto T^2$ at high temperatures, and $T_1^{-1} \propto T^9 J_8(\Theta/T)$ at intermediate temperatures. Computation of the transport integrals for noninteger values of n is discussed in the Appendix.

IV. FRACTAL DIMENSION

In common usage a geometric figure is often said to be d-dimensional if d is the minimum number of parameters required to specify the location of all the points that make up the figure. For example, two parameters may be needed to specify the location of a point in the interior of a square, hence a square is two dimensional. This definition was shown to be inadequate toward the end of the 19th century when G. Peano (28) demonstrated a continuous mapping from the real line to an area in two-dimensional space. This continuous curve passes through every point in the area, and consequently allows every point in the area to be specified by one parameter, the distance along the curve. Several rigorous definitions of dimensionality have been developed (29) to overcome this difficulty. A particularly simple and useful definition is the "fractal" dimension (2).

The fractal dimension is defined for those objects that exhibit self-similarity. A self-similar object is invariant under a transformation of scale. The unit square in the plane is self-similar. When all lengths ℓ are scaled by a factor $s = 2$, the square remains identical to the original, except for size, and four of the scaled squares stacked together produce an object identical to the original square. The fractal definition of dimension, d, relates the number, n, of copies of a scaled object needed to cover the original to the scale factor, s, by the relation

$$n \propto s^d. \quad (10)$$

In the example of the square, $d = 2$, in agreement with intuition.

The definition of fractal dimension requires objects to have a regularity seldom found in nature. The definition can, however, be extended to irregular figures through the concept of statistical self-similarity, when some statistical distribution function describing the properties of the object (rather than the object itself) exhibits self-similarity. An example of some significance in the present work is the random walk in two or more dimensions, that exhibits the property of self-similarity, and that can therefore be assigned a fractal dimension. The components of the vectors connecting points on a random walk N steps apart are Gaussian random variables of mean zero and standard deviation $\sigma(N) = \ell N^{1/2}$, where ℓ is the step size. It is easily shown that the standard deviation of the vectors connecting points N/n steps apart in a walk of step size ℓ is the same as the standard deviation of the vectors connecting points N steps apart in a walk of scaled down steps, ℓ/s in size, where $s = n^{1/2}$. That is

$$\sigma_1(N) = \sigma_0(N/n) = n^{1/2}\sigma_0(N), \quad (11)$$

where the subscripts 0 and 1 refer to the original and scaled walks, respectively. Because n of the scaled vectors cover the original, the fractal dimension is obtained from Eq. 10 in the form

$$d = \log(n)/\log(s) = \log(n)/\log(n^{1/2}) = 2. \quad (12)$$

The self-avoiding random walk is similar to the random walk except that the curve is constrained to avoid self-intersection. It is often used as a model for polymers. The constraint on self-intersection prevents the curve from reaching certain regions of space and complicates a calcu-

lation of the dimensionality. No exact expression for this quantity has been discovered. Renormalization group theory methods (30, 31) and numerical experiments (32, 33) yield values of the fractal dimension of a self-avoiding random walk in E3 that are within 2% of 5/3.

A simple example will best show how the fractal dimension of a structure is calculated. Fig. 5 contains a curve in two-dimensional Euclidean space (E2) known as a Koch island (2), Its fractal dimension of 5/3 can be computed knowing that $n = 32$ and $s = 8$. To compute d numerically, one would draw circles of various radii R about an arbitrary point on the curve. From this origin, proceeding in both directions, the total number n of steps would then be counted until the curve cuts the circle at radius R. The results, defining the variations of n with R, would then be fit to a power law $n \propto R^d$. The upper portion of Fig. 5 makes clear which elements are counted for the circles indicated. Using this method, and averaging the results from various origins evenly distributed throughout the structure, one would find a fractal dimension of 1.66 ± 0.01 for the Koch island, in good agreement with the exact value of 5/3. (Note that if, by error, all elemental steps within each circle are counted, including those from the reentrant portions of the curve, the calculated d is 6% smaller than 5/3.) A similar error with protein structures can cause 35% discrepancies.

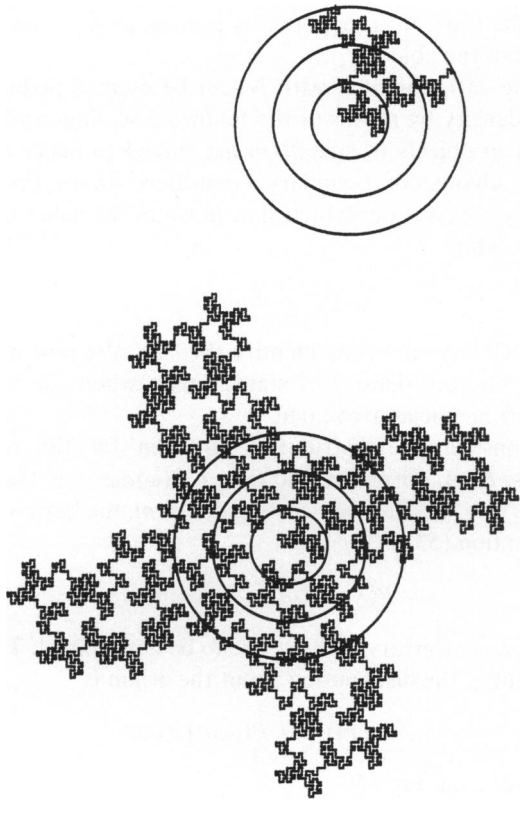

FIGURE 5. The lower curve represents a Koch island ($N = 32, S = 8, d = 5/3$) in a two-dimensional Euclidean space with a series of circles centered at an arbitrary element of the curve. The upper figure shows only those elements that should be counted within each circle when computing the fractal dimensionality according to the method described in the text.

Proteins lack rigorous self-similarity but a value of d can nevertheless be obtained from x-ray data (34–51) by drawing spheres of radius R about an arbitrary α-carbon on the polypeptide backbone, and counting the number of α-carbons to the intersection, as in the example provided above. The resulting value of d depends somewhat on our choice of an origin; the results were therefore averaged over various origins evenly distributed throughout the entire backbone. To eliminate end effects, the procedure was terminated whenever either end of the backbone was found within the sphere and whenever the number of points exceeded a specified maximum N. The fractal dimensions found in this way for 17 proteins are listed in Table II, with the minimum value of N for which d remains within the listed standard error. As a check against any systematic error, d was calculated for Mb using independent sets of x-ray data at different temperatures. The resulting changes in d were <0.02, well within the listed standard error of ± 0.04 for Mb.

The data of Table II indicate that the hemoproteins Mb, cyt c, and the alpha and beta chains of hemoglobin (Hb) all have fractal dimensions close to 5/3. This is the value associated with a SAW3. Our relaxation data on hemoproteins are consistent with this value of d because $d = 5/3$ leads to a Raman rate that varies with temperature as $T^{6.333}$. Fig. 6 gives conventional ($d = 3$) Raman fits of the pulse-saturation/recovery data from Fig. 1. Debye temperatures near 55 K are required, and the theoretical result exhibits a curvature that is not apparent in the data.

TABLE II
FRACTAL DIMENSIONS OF SOME SELECTED PROTEINS

Protein	Fractal dimension d	N_{min}	References
Myoglobin (ferric)	1.66 ± 0.04	115	35
Cytochrome *c* (ferric)	1.66 ± 0.05	80	36
Ferredoxin	1.34 ± 0.05	30	37
Hemoglobin (alpha, ferric)	1.64 ± 0.03	90	38
Hemoglobin (beta, ferric)	1.62 ± 0.04	90	38
Cytochrome *c*550 (ferrous)	1.69 ± 0.05	90	39
Cytochrome *c*551 (ferric)	1.47 ± 0.04	45	40
Cytochrome *c*2 (ferric)	1.71 ± 0.05	80	41
Cytochrome *b*5 (ferric)	1.62 ± 0.06	70	42
Lysozyme	1.76 ± 0.05	90	43
Trypsin (Ca^{2+})	1.54 ± 0.05	120	44
Carboxypeptidase A (Zn^{2+})	1.56 ± 0.04	130	45
Papain	1.76 ± 0.06	115	46
Ribonuclease s	1.35 ± 0.05	55	47
Chymotrypsin alpha	1.36 ± 0.05	95	48
Chymotrypsin gamma	1.35 ± 0.05	70	49
Rubredoxin (ferric)	1.49 ± 0.06	35	50
HiPIP (8 iron/sulfur)	1.52 ± 0.05	45	51

The fractal dimension of several proteins based upon x-ray structural data and the computational method described in the text. Also listed are the minimum values of the parameter N for which d remains within the listed standard error.

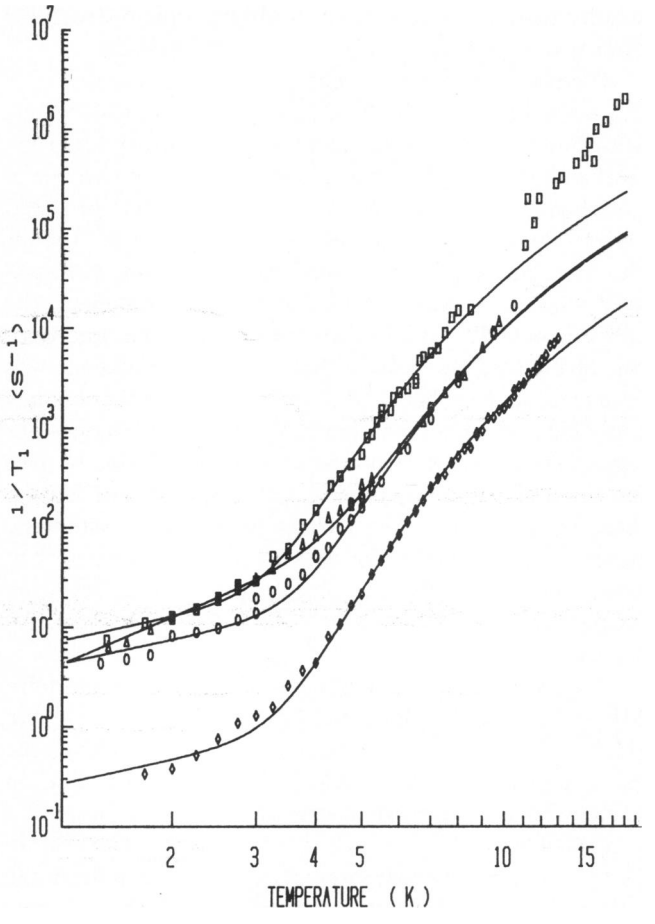

FIGURE 6 A conventional (d = 3) Raman fit of the pulse-saturation/recovery data ($1/T_1 \leq 10^4\ s^{-1}$) of Fig. 1. Debye temperatures near 55 K are required to reduce the effective log-log slope from 9 to 6.33, and this causes the curves to fall short of the data at higher temperatures. Refer to the caption of Fig. 1 for a designation of the undisplayed data. □, cyt c, $6.34T$ + 0.129E-7 $T^9 J_8(48.1/T)$; Δ, Mb, 3.15 T^2 + 0.242E-8 T^9 $J_8(53.6/T)$; O, MbN_3, 3.73 T + 0.240E-8 T^9 J_8 (54.3/T); ◇, $P450$, $0.230T$ + 0.347E-9 T^9 J_8 (57.0/T).

Ferredoxin differs from the case of heme proteins. Its fractal dimension is $d = 1.34 \pm 0.05$ from x-ray data, and $d = 1.34 \pm 0.06$ from the relaxation data of Gayda et al. (5) (see Fig. 2).

We note that the distribution of α-carbons in proteins has been examined by DeSantis et al. (52). These authors determine the total number of α-carbons within spheres, without restriction. These results are then displayed in an interesting way as a function of R'^3 where R' corresponds, not to real space, but to a space that has been transformed in such a way that the α-carbons are redistributed isotropically. Unfortunately, the fractal dimension measures the distribution of the backbone in real space and the fractal properties that play an important role in the present work were therefore overlooked in the earlier research.

V. VIBRATIONAL DENSITY OF STATES

It is, of course, well known that the density of vibrational states $\rho(\omega)$, varies as ω^{d-1} when d corresponds to a Euclidean dimension of 3, 2, or 1. We now show that this result remains valid for arbitrary fractal dimension d.

We present here an elaboration of our earlier proof (1). Suppose that an elastic object consists of N identical units of mass M, linked to form a body that is homogeneous and isotropic. Its linear extent L is given by $L^d \propto N$, where d is, by definition, the fractal dimensionality of the object. For a small bulk deformation that maps the body onto its analog of volume $N(1-\epsilon)$, the decrease of length ΔL is $\Delta L = L\epsilon/d$; the elastic energy is $Nc\epsilon^2/2$, with c the appropriate elastic constant describing each element in proportion to the number of elements and the elongation squared.

Consider now the configuration space of the N units. In this space, the deformation described above is a straight line along some axis. The elastic energy is a function of the displacement, ξ, from the potential minimum and is $M\omega^2\xi^2/2$ with ω the lowest vibrational normal mode frequency. A new change to cyclic boundary conditions of the object will make each element project equally on ξ. Suppose this projection has the value ΔL. Then use of the N-dimensional Pythagorean Theorem gives $\xi^2 \propto N(\Delta L)^2 \propto NL^2\epsilon^2$, and hence, by equating the expressions for the elastic energy, one obtains

$$\omega \propto (c/M)^{1/2}L^{-1} \propto (c/M)^{1/2}N^{-1/d}. \quad (13)$$

This expression is physically reasonable because it shows that the time of propagation is proportional to the linear extent of the object.

The variation of ω with N can be used to deduce the state density by means of the following scaling argument. When m objects of size N/m are linked to make N, the minor change of boundary conditions leaves the total density of states unperturbed at m times the value for one object. Thus

$$\rho_N(\omega) = m\rho_{N/m}(\omega), \quad (14)$$

in which the subscripts identify the size. We now need to show how the density of states varies when the normal mode frequencies are scaled.

Consider the distribution function for the normal modes, $P(\omega)$, normalized so that $\int P(\omega)d\omega = 1$. Defining $P(\omega,m) \equiv P_{N/m}(\omega)$ for a scaling factor m, the basic scaling assumption (53) is

$$P(\lambda^a\omega,\lambda^b m) = \lambda P(\omega,m), \quad (15)$$

where λ is arbitrary and a, b are to be determined. The tth moment of the distribution about the origin is

$$\mu(t,m) = \int P(\omega,m)\omega^t d\omega. \quad (16)$$

Whence from Eq. 15

$$\mu(t,\lambda^b m) = \int P(\lambda^a\omega,\lambda^b m)(\lambda^a\omega)^t d(\lambda^a\omega) = \lambda^{at+a+1}\mu(t,m). \quad (17)$$

Because λ is an arbitrary parameter, we may set $\lambda = m^{-1/b}$.

Then

$$\mu(t,1) = m^{-(at+a+1)/b}\mu(t,m). \quad (18)$$

But the distribution function is normalized and therefore, setting $t = 0$, $\mu(0,1) = 1$. It follows that $a = -1$, and thus from Eq. 15

$$P(\omega/\lambda,\lambda^b m) = \lambda P(\omega,m). \quad (19)$$

With λ still arbitrary, one may again set $\lambda = m^{-1/b}$ to find

$$\rho_{N/m}(\omega) = m^{1/b}\rho_N(m^{1/b}\omega). \quad (20)$$

The value of b is now determined from the N dependence of ω in Eq. 13, where a scale change described by Eq. 20 produces a frequency change by a factor of $m^{-1/d}$. Thus $b = -d$. The factor of $m^{-1/d}$, on the right of Eq. 20 takes account of a reduction of the frequency interval between normal modes caused by the size change. With

$$\rho_{N/m}(\omega) = m^{-1/d}\rho_N(\omega m^{-1/d}) \quad (21)$$

Eq. 14 now yields

$$\rho_N(\omega) = m^{1-1/d}\rho_N(\omega m^{-1/d}), \quad (22)$$

and the substitution of an ω^p power law for $\rho(\omega)$ gives $p = d-1$, which is the desired result. The variation of $\rho(\omega)$ as ω^{d-1} therefore holds for arbitrary fractal dimension d. Note that the convenient boundary conditions from which Eq. 13 is derived do not change $\rho(\omega)$ but merely shift the spectrum of eigenvalues by part of the mode spacing.

VI. LINE-WIDTH DATA

There are numerous pitfalls to avoid in any measurement of T_1 from the temperature dependence of the line broadening, and the problems increase when measurements must be made on powdered crystals or frozen solutions. The techniques used to obtain the ferredoxin relaxation rates at temperatures >46 K, are described by Bertrand et al. (54). It is often assumed that $T_1 = T_2$ when the line width is dominated by lifetime broadening, and this approximation was one made in the ferredoxin work. In general, however, the T_2/T_1 ratio under these conditions depends upon the nature of the paramagnetic ion (Kramers or non-Kramers) and on the relaxation process involved. Theoretical papers by Culvahouse and Richards (55) and Stedman (56, 57) deal with the complexities of this problem. The Weisskopf-Wigner (58, 59) relationship indicates that the full width at half maximum $2/T_2$ is the sum of the transition rates out of the two states involved in the absorption line, i.e.,

$$2/T_2 = W_a + W_b, \quad (23)$$

where a and b denote the two states of the doublet. For the direct process $W_a + W_b$ is equal to $1/T_1$ by definition, so that the usual NMR expression of Bloembergen (60)

$$1/T_2 = 1/T_2' + 1/2T_1 \quad (24)$$

for the T_1 contribution to T_2 holds when spin-spin (T_2') contributions to the line width are included.

Second-order processes make a calculation of T_2/T_1 complicated because the possibility of self-energy contributions exist in which the initial and final spin states remain the same, while the phonon states change. This can occur with real intermediate states, as in the Orbach process, or with the virtual intermediate states of the Raman mechanism.

For an Orbach process involving a Kramer's ion for which the energy levels and transition frequencies are well separated, the pertinent relationships are (55)

$$\frac{1}{T_1} = \frac{4B_1B_2}{(B_1 + B_2)} \frac{1}{e^{\Delta/T}-1}, \quad (25)$$

and

$$\frac{1}{T_2} = \frac{(B_1 + B_2)}{e^{\Delta/T}-1},$$

where B_1 and B_2 involve different matrix elements. It is possible to have a phonon bottleneck in the Orbach process; this has no effect on T_2, but it reduces the value of $1/T_1$ measured by pulse-saturation/recovery (55, 61).

For Kramer's ions, the self-energy terms of the nonresonant Raman process apparently vanish and $2/T_2 = 1/T_1$. For a non-Kramer's T^7 Raman process, $2/T_2 = 1/T_1 + \Gamma$ where Γ is the self-energy contribution. Kemple and Stapleton (62) have estimated T_2/T_1 to lie between 0.9 and 1.8 for such a process in Ho^{3+}-doped yttrium ethyl sulfate.

Fig. 7 shows the ferredoxin data over the temperature range from 1.225 to 132 K. Relaxation rates for temperatures >46 K were obtained from line width studies. Curve *1* corresponds to the fit reported by the original investigators (5) to the form

$$1/T_1 = 0.9\,T^2 + 3.5\,10^{-10}\,T^9 J_8(60/T) + 7.3\,10^{10}\,e^{-350/T}. \quad (26)$$

This fit assumes a conventional ($d = 3$) Raman process and requires a Debye temperature of 60 K to reduce the slope of the log-log plot from 9 to agree better with the experimental value of 5.67. The low value of $\Theta = \hbar\omega_{max}/k_B = 60$ K in turn requires that the Orbach relaxation mechanism involve a localized vibrational mode. Curve *2*, which has the form

$$1/T_1 = 0.874\,T^2 + 0.00341\,T^{5.666} + 4.40\,10^{10}\,e^{-348/T}, \quad (27)$$

fits the data equally well. It eliminates the need to invoke local vibrational modes because no Debye temperature is required, and it can be assumed to exceed 348 K. It is interesting to attempt to fit the data of Fig. 7 without the inclusion of an Orbach relaxation term. The data are then

equally well fit by the function

$$1/T_1 = 0.865\ T^2 + 4.94\ 10^{-5} T^{5.666} J_{4.666}(610/T), \quad (28)$$

if all the relaxation rates derived from line width data are reduced by a factor of 0.2404 and a Debye temperature of 610 K is included in the appropriate transport integral. It is unlikely that such a reduction is proper because a dominant Raman relaxation mechanism >46 K requires that all the relaxation rates obtained from line width data in Fig. 7 be doubled, not reduced by a factor 4. By contrast, a dominant Orbach relaxation mechanism implies that the line width data of Fig. 7 are either correct or too high since the T_2/T_1 ratio in that case can lie anywhere between 0 and 1 depending upon the unknown value of two matrix elements.

VII. CONCLUSION

In this paper we have presented experimental and theoretical evidence that a fractal model provides an excellent description of the Raman relaxation mechanism in proteins. The model predicts that the Raman process will vary with T as T^{3+2d} at low temperature, with d the fractal dimension of the protein. Computation of d is simple if the protein structure is known; it is strongly influenced by the protein configuration. We have outlined a procedure for calculating d and have tabulated its value for several paramagnetic and diamagnetic native proteins. These values fall in the range between 4/3 and 7/4, which is reasonable when compared to the theoretical result d = 5/3 for a self-avoiding random walk in three dimensional Euclidean space. Structures that differ substantially in detail can, however, share the same fractal dimension, so that no randomness of protein structures is implied by this result. We have not yet established that this model of spin relaxation in proteins is valid for ions other than iron attached to the protein; nor have we determined when this relaxation process will be dominant.

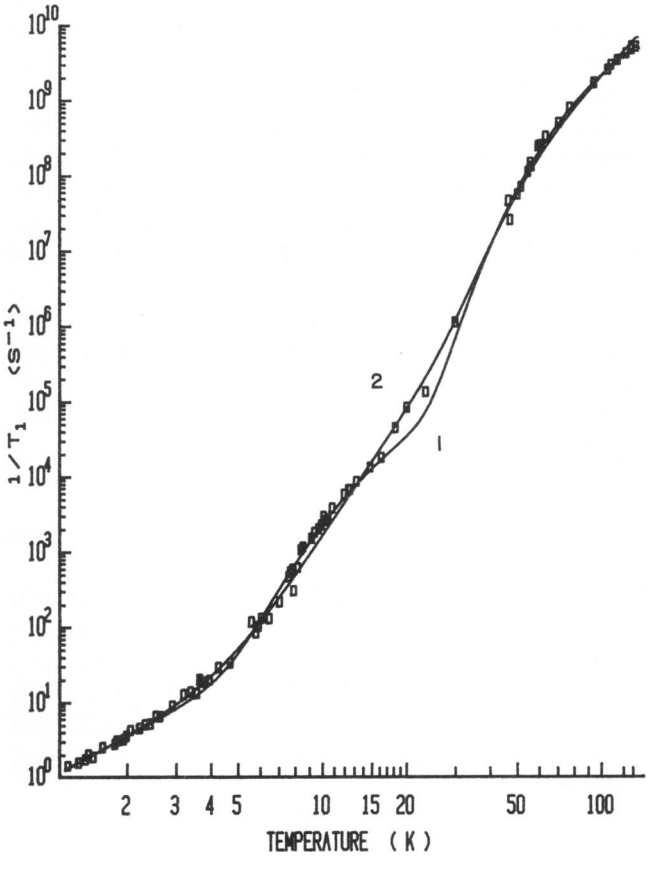

FIGURE 7 Complete ferredoxin data, from reference 5, including line width data taken between 46 and 132 K. Curve *1* is that reported by the authors and involves a conventional (d = 3) Raman fit with a Debye temperature of 60 K and an Orbach process involving a localized vibrational mode with an energy of 350 K. Curve *2* is our fit of the data with a fractal Raman process (d = 4/3) as determined from x-ray data, and an Orbach process with an excited state energy of 348 K.

It has proved possible to calculate values of d from spin-lattice relaxation rates or from x-ray results, with an uncertainty in each case of ~3%. The mean values obtained by the two different techniques agree within 0.6% while the values of d vary among the different proteins by 20%. These results constitute a remarkable confirmation of the theory because the determinations of d require no adjustable parameters.

Our results lead us to suggest finally that low temperature spin-relaxation measurements can be used in future experiments as a sensitive probe for small changes in protein (or other molecular) conformation. The need for detailed x-ray analysis can therefore be eliminated in appropriate cases.

To provide a useful probe, the paramagnetic species in the spin system must relax via a dominant Raman process over a reasonably large temperature interval at low temperature. No conformational information can be obtained if an Orbach process is dominant. If the measurements are taken at excessively high temperatures, the Raman relaxation rate will vary more slowly than T^{3+2d}, eventually approaching the classical T^2 limit of a two phonon process. The systems analyzed in this paper contain only low-spin iron, with no Orbach process; or antiferromagnetically coupled $Fe^{2+} - Fe^{3+}$, for which a weak Orbach process may be present.

APPENDIX

Modified Transport Integrals

Following the development of Rogers and Powell (27), we have computed the values for the transport integral for noninteger n. These are required for the experimental determination of the appropriate Debye temperature. An integration by parts gives

$$J_n(x) = \frac{-x^n}{e^x - 1} + n \int_0^x \frac{z^{n-1} dz}{e^z - 1}. \quad (A1)$$

For large values of x, the integral term is rewritten by separating it into two integrals and expanding the denominator yielding

$$J_n(x) = \frac{-x^n}{e^x - 1} + n\Gamma(n)\zeta(n) - n\sum_{s=1}^{\infty}\int_x^{\infty} z^{n-1}e^{-sz}\,dz. \quad \text{(A2)}$$

The limiting value as x increases without limit is $n\Gamma(n)\zeta(n)$. For noninteger n, the third term of Eq. A2 cannot be written as a simple series but rather the integral was computed directly using a gaussian quadrature approximation. For small values of x, both terms of Eq. A1 may be rewritten, using a Bernoulli Expansion that for $x < 2\pi$ gives

$$J_n(x) = x^{n-1}\left[\frac{1}{n-1} - \sum_{s=1}^{\infty}(-1)^{s-1}\frac{B_s(2s-1)x^{2s}}{(2s)!\,(n+2s-1)}\right], \quad \text{(A3)}$$

where B_s are the Bernoulli numbers. The limiting asymptotic value as x approaches zero is

$$\lim_{x\to 0} J_n(x) = \frac{x^{n-1}}{n-1}. \quad \text{(A4)}$$

This work was supported in part by the U. S. Public Health Service under grant No. GM-24488. Use was made of the DEC 20/60 (Digital Equipment Corp.) computer facility of the Materials Research Laboratory.

Received for publication 15 October 1981 and in revised form 29 January 1982.

REFERENCES

1. Stapleton, H. J., J. P. Allen, C. P. Flynn, D. G. Stinson, and S. R. Kurtz. 1980. Fractal form of proteins. *Phys. Rev. Lett.* 45:1456.
2. Mandelbrot, B. B. 1977. Fractals: Form, Chance, and Dimension. Freeman Publications, San Francisco. 1456–1459.
3. Mailer, C., and C. P. S. Taylor. 1973. Rapid adaibatic passage EPR of ferricytochrome *c*: signal enhancement and determination of the spin-lattice relaxation time. *Biochim. Biophys. Acta.* 322:195–203.
4. Herrick, R. C., and H. J. Stapleton. 1976. Anomalous T^7 Raman spin-lattice relaxation rate of low spin cytochrome P-450 from *Pseudomonas putida*. *J. Chem. Phys.* 65:4778–4785.
5. Gayda, J. P., P. Bertrand, A. Deville, C. More, G. Roger, J. F. Gibson, and R. Cammack. 1979. Temperature dependence of the electronic spin-lattice relaxation time in a 2-iron-2-sulfur protein. *Biochim. Biophys. Acta.* 581:15–26.
6. Stevens, K. W. H. 1975. The theory of paramagnetic relaxation. *Rep. Progr. Phys.* 30:189–226.
7. Orbach, R., and H. J. Stapleton. 1972. Electron spin-lattice relaxation. *In* Electron Paramagnetic Resonance. S. Geschwind, editor. Plenum Publishing Corp., New York.
8. Gill, J. C. 1975. The establishment of thermal equilibrium in paramagnetic crystals. *Rep. Progr. Phys.* 38:91–150.
9. Stapleton, H. J. 1972. Electron spin relaxation. *Magnetic Resonance Review.* 1:65–89.
10. Bray, T., G. C. Brown, Jr., and A. Kiel. 1962. Paramagnetic relaxation of Fe^{3+} in potassium cobalticyanide. *Phys. Rev.* 127:730–737.
11. Rannestad, A., and P. E. Wagner. 1963. Paramagnetic relaxation in dilute potassium ferricyanide. *Phys. Rev.* 131:1953–1960.
12. Scott, P. L., and C. D. Jeffries. 1962. Spin-lattice relaxation in some rare-earth salts at helium temperatures; observation of the phonon bottleneck. *Phys. Rev.* 127:32–51.
13. Mikkelson, R. C., and H. J. Stapleton. 1965. Anisotropic spin-lattice relaxation rates of some rare-earth-doped lanthanum trichlorides. *Phys. Rev. A.* 140:1968–1982.
14. Kurtz, S. R., and H. J. Stapleton. 1980. Effects of disorder on electron-spin relaxation in β-alumma: a prototype glass. *Phys. Rev. B.* 22:2195–2205.
15. Singh, G. P., F. Parak, S. Hunklinger, and K. Dransfeld. 1981. Role of adsorbed water in the dynamics of metmyoglobin. *Phys. Rev. Lett.* 47:685–688.
16. Theorell, H., and A. Akesson. 1941. Studies on cytochrome *c*. II. The optical properties of pure cytochrome *c* and some of its derivatives. *J. Am. Chem. Soc.* 63:1812–1818.
17. Dickerson, R. E., and R. Timkovich. 1975. Cytochromes *c*. *In* The Enzymes. Paul D. Boyer, editor. 11:397. Academic Press, Inc., New York.
18. Gordon, J. D. 1961. Variable coupling reflection cavity for microwave spectroscopy. *Rev. Sci. Instrum.* 32:658–661.
19. Yonetani, T., and H. Schleyer. 1967. Electromagnetic properties of hemoproteins. *J. Biol. Chem.* 242:3926–3933.
20. Gurd, F. R. N., K.-E. Falk, B. G. Malmstrom, and T. Vanngard. 1967. A magnetic resonance study of sperm whale ferrimyoglobin and its complex with 1 cupric ion. *J. Biol. Chem.* 242:5724–5730.
21. Morton, R. A., and T. L. Bohan. 1971. The electron paramagnetic resonance spectrum at 77°K of lyophilized and frozen solutions of horse heart ferricytochrome *c*. *Can. J. Biochem.* 49:328–331.
22. Lambeth, D. O., K. L. Campbell, R. Zand, and G. Palmer. 1973. The appearance of transient species of cytochrome *c* upon rapid oxidation or reduction at alkaline pH. *J. Biol. Chem.* 248:8130–8136.
23. Marchand, R. L., and H. J. Stapleton. 1974. Observation of an $H^2T^7\sin^2\theta$ Raman spin-lattice relaxation rate in a neodynmium salt. *Phys. Rev. B.* 9:14–21.
24. Ablart, G., P. Boujol, P. Lopez, and J. Pescia. 1975. Observation of a spin-lattice relaxation rate dependent on the magnetic field in $CuCl_2\,2H_2O$. *Solid State Commun.* 17:1085–1088.
25. Orbach, R., and M. Tachiki. 1967. Phonon-induced ion-ion coupling in paramagnetic salts. *Phys. Rev.* 158:524–529.
26. Abragam, A., and B. Bleaney. 1970. Electron Paramagnetic Resonance of Transition Ions. Clarendon Press, Oxford.
27. Rogers, W. M., and R. L. Powell. 1958. Tables of Transport Integrals. *Nat. Bur. Stand. (U.S.) Circ.* 1–595.
28. Peano, G. 1890. Sur une courbe, qui remplir une aire plane. *Mathematische Annalen.* 36:157. Translated in Peano, G. 1973. Selected Works. H. C. Kennedy, editor. University of Toronto Press, Toronto. 157–160.
29. Hurcwicz, W., and A. Wallman. 1941. Dimension Theory. Princeton University Press, Princeton.
30. De Gennes, P. G. 1972. Exponents for the excluded volume problem as derived by the Wilson method. *Phys. Lett. A.* 38:339–340.
31. Kremer, K., A. Baumgartner, and K. Binder. 1981. Monte Carlo renormalization of hard sphere polymer chains in two to five dimensions. *Z. Phys. B.* 40:331–341.
32. Le Gillou, J. C., and J. Zinn-Justin. 1977. Critical exponents for the *n*-vector model in three dimensions from field theory. *Phys. Rev. Lett.* 39:95–98.
33. Barr, R., C. Brender, and M. Lax. 1980. Self-avoiding walks with span limitations. I. The mean square end-to-end distance. *J. Chem. Phys.* 72:2702–2707.
34. Bernstein, F. C., T. F. Koetzle, G. J. B. Williams, E. F. Meyer, Jr., M. D. Brice, J. R. Rodgers, O. Vennard, T. Shimanouchi, and M. Tasumi. 1977. The protein data bank: a computer-based archival file for macromolecular structures. *J. Mol. Biol.* 112:535–542.
35. Watson, H. C. 1969. The stereochemistry of the protein myoglobin. *Progr. Stereochem.* 4:299–333.
36. Swanson, R., B. L. Trus, N. Mandel, G. Mandel, O. B. Kallai, and R. E. Dickerson. 1977. Tuna cytochrome *c* at 2.0 Angstroms resolution, ferricytochrome structure analysis. *J. Biol. Chem.* 252:759–785.
37. Adman, E. T., L. C. Sieker, and L. H. Jensen. 1976. Structure of *Peptococcus aerogenes* ferredoxin, refinement at 2 Angstroms resolution. *J. Biol. Chem.* 251:3801–3806.
38. Ladner, R. C., E. G. Heidner, and M. F. Perutz. 1977. The structure of horse methaemoglobin at 2.0 Angstroms resolution. *J. Mol. Biol.* 114:385–414.

39. Timkovich, T., and R. E. Dickerson. 1976. The structure of paracoccus denitrificans cytochrome *c* 550. *J. Biol. Chem.* 251:4033–4046.
40. Almassy, R. J., and R. E. Dickerson. 1978. Pseudomonas cytochrome *c* 551 at 2.0 Angstroms resolution. Enlargement of the cytochrome *c* family. *Proc. Natl. Acad. Sci. U. S. A.* 75:2674–2678.
41. Salemme, F. R., S. T. Freer, N. H. Xuong, R. A. Alden, and J. Kraut. 1973. The structure of oxidized cytochrome c2 of rhodospirillum rubrum. *J. Biol. Chem.* 248:3910–3921.
42. Mathews, F. S., P. Argos, and M. Levine. 1972. The structure of cytochrome b_5 at 2.0 Angstroms resolution. *Cold Spring Harbor Symp. Quant. Biol.* 36:387–395.
43. Diamond, R. 1974. Real-space refinement of the structure of hen egg-white lysozyme. *J. Mol. Biol.* 82:371–391.
44. Fehlhammer, H., and W. Bode. 1975. The refined crystal structure of bovine beta-trypsin at 1.8 Angstroms resolution. *J. Mol. Biol.* 98:683–692.
45. Quiocho, F. A., and W. N. Lipscomb. 1971. Carboxypeptidase A, a protein and an enzyme. *Adv. Protein Chem.* 25:1–78.
46. Drenth, J., J. N. Jansonius, R. Koekoek, H. M. Swen, and B. G. Wolthers. 1968. Structure of papain. *Nature (Lond.).* 218:929–933.
47. Fletterick, R. J., and H. W. Wyckoff. 1975. Preliminary refinement of protein coordinates in real space. *Acta Crystallogr. Sect. A.* 31:698–700.
48. Birktoft, J. J., and D. M. Blow. 1972. The structure of crystalline alpha-chymotrypsin, the atomic structure of tosyl-alpha-chymotrypsin at 2 Angstroms resolution. *J. Mol. Biol.* 68:187–240.
49. Segal, D. M., G. H. Cohen, D. R. Davies, J. C. Powers, and P. E. Wilcox. 1972. The stereochemistry of substrate binding to chymotrypsin A gamma. *Cold Spring Harbor Symp. Quant. Biol.* 36:85–90.
50. Watenpaugh, K. D., L. C. Sieker, J. R. Herriott, and L.H. Jensen. 1973. Refinement of the model of a protein: rubredoxin at 1.5 Angstroms resolution. *Acta Crystallogr. Sect. B.* 29:943–956.
51. Carter, C. W., Jr., J. Kraut, S. T. Freer, N.-H. Xuong, R. A. Alden, and R. G. Bartsch. 1974. Two-Angstrom crystal structure of oxidized chromatium high potential iron protein. *J. Biol. Chem.* 249:4212–4225.
52. Desantis, P., S. Morosetti, and A. Palleschi. 1979. Moments of the distribution of the amino acid residues in tertiary structures of globular proteins. *Biopolymers.* 18:2963–2978.
53. McKenzie, D. S. 1976. Polymers and scaling. *Phys. Reports.* 27:35–88.
54. Bertrand, P., G. Roger, and J. P. Gayda. 1980. Measurement of the spin-lattice relaxation time from the broadening of the EPR spectrum of a randomly oriented system with $S = 1/2$: application to iron-sulfur proteins. *J. Magn. Reson.* 40:539–549.
55. Culvahouse, J. W., and P. R. Richards. 1969. T_1 and T_2 for Orbach relaxation processes. *Phys. Rev.* 178:485–497.
56. Stedman, G. E. 1970. Raman ion-lattice interaction processes and the linewidth problem. *J. Phys. C*3:2392–2401.
57. Stedman, G. E. 1971. Validity of the Weisskopf-Wigner linewidth-lifetime relaxation for spectral lines broadened by phonon interaction. *J. Phys. C*4:1022–1035.
58. Weisskopf, V., and E. Wigner. 1930. Berechnung der naturlichen Linienbreite auf Grund der Diracschen Lichttheorie. *Z. Phys.* 63:54–73.
59. Weisskopf, V., and E. Wigner. 1930. Uber die naturliche Linienbreite in der Strahlung des harmonischen Oszillators. *Z. Phys.* 65:18–29.
60. Bloembergen, N. 1948. Nuclear magnetic relaxation. Ph.D. dissertation, Utrecht.
61. Stapleton, H. J., and K. L. Brower. 1969. Electron spin resonance linewidth variation with temperature in some rare-earth salts: T_1/T_2 ratios. *Phys. Rev.* 178:481–485.
62. Kemple, M. D., and H. J. Stapleton. 1972. Spin-lattice relaxation of Ho^{3+} in yttrium ethyl sulfate between 1.2 and 25 K. *Phys. Rev. B*5:1668–75.